

Engineering a Multi-Mode Purcell Filter for Superconducting-Qubit Reset and Readout with Intrinsic Purcell Protection

Xu-Yang Gu,^{1,2,*} Da'er Feng,^{1,2,*} Zhen-Yu Peng,^{1,2} Gui-Han Liang,^{1,2} Yang He,^{1,2}
Yongxi Xiao,^{1,2} Ming-Chuan Wang,^{1,2} Yu Yan,^{1,3} Bing-Jie Chen,^{1,2} Zheng-Yang Mei,^{1,2}
Yi-Zhou Bu,^{1,2} Jia-Chi Zhang,^{1,2} Jia-Cheng Song,^{1,2} Cheng-Lin Deng,^{1,2} Xiaohui Song,¹
Dongning Zheng,^{1,2,4,5} Kai Xu,^{1,2,6,4,5,†} Zhongcheng Xiang,^{1,2,4,‡} and Heng Fan^{1,2,6,4,5,§}

¹*Beijing National Laboratory for Condensed Matter Physics,*

Institute of Physics, Chinese Academy of Sciences, Beijing 100190, China

²*School of Physical Sciences, University of Chinese Academy of Sciences, Beijing 100049, China*

³*School of Physics, Northwest University, Xi'an 710127, China*

⁴*Hefei National Laboratory, Hefei 230088, China*

⁵*Songshan Lake Materials Laboratory, Dongguan, Guangdong 523808, China*

⁶*Beijing Key Laboratory of Fault-Tolerant Quantum Computing,
Beijing Academy of Quantum Information Sciences, Beijing 100193, China*

Efficient qubit reset and leakage reduction are essential for scalable superconducting quantum computing, particularly in the context of quantum error correction. However, such operations often require additional on-chip components. Here, we propose and experimentally demonstrate a mode-efficient approach to qubit reset and readout using a multi-mode Purcell filter in a superconducting quantum circuit. We exploit the inherent multi-mode structure of a coplanar waveguide resonator, using its fundamental and second-order modes for qubit reset and readout, respectively, thereby avoiding additional circuit elements. Implemented in a flip-chip architecture, our device achieves unconditional reset with residual excitation below 1% in 220 ns, and a leakage reduction unit that selectively resets the second excited state within 62 ns. Simulations predict Purcell-limited relaxation times exceeding 1 ms over an 800 MHz bandwidth. To our knowledge, this is the first experimental trial that exploits different-order modes of a microwave resonator for distinct qubit operations, representing a new direction toward scalable, mode-efficient quantum processor design.

I. INTRODUCTION

Fault-tolerant superconducting quantum computing requires sophisticated manipulation of over million physical qubits [1]. To advance toward this goal, two complementary directions have attracted considerable attention. One involves the development of distributed quantum network architectures [2–12], while the other focuses on maximizing the number of physical qubits integrated on a single chip. Achieving the latter requires minimizing the number of on-chip components while maintaining sufficient controllability of the qubits. However, enhanced controllability often requires additional physical components on the chip. For example, implementing operations such as fast unconditional reset [13–18] and leakage reduction unit (LRU) [15, 17, 19–22], which are useful in schemes like quantum error correction [1, 23–27], typically requires a dedicated dissipative channel whose frequency lies below the qubit frequency [17, 18, 22]. Despite the existence of several alternative approaches, such as repurposing the readout resonator as a reset channel by placing its frequency below the qubit band [13, 15], employing parametrically activated interactions [16], or utilizing cavity-assisted Raman transitions [14],

each comes with its own limitations. The latter two typically require complex calibration and are sensitive to noise and parameter drift, while the former may introduce undesired effects such as measurement-induced mixing [28].

To realize qubit reset and leakage reduction operations without introducing additional on-chip components, we propose assigning multiple functions to a single physical element. For example, a coplanar waveguide resonator is inherently a multi-mode system, supporting a fundamental mode at frequency f_0 and higher-order harmonics at $f_m = (m + 1)f_0$. Harnessing these different-order modes for distinct qubit operations offers a promising route toward improving circuit scalability. In this work, we design and experimentally demonstrate a multi-mode Purcell filter, where the fundamental mode is used for qubit reset and the second-order mode for readout. To the best of our knowledge, this is the first experimental realization that exploits different-order modes of a microwave resonator to implement distinct qubit operations. This approach represents a significant step toward mode-efficient circuit design and scalable superconducting quantum architectures.

The proposed scheme is implemented by coupling the qubit and its readout resonator to a multi-mode Purcell filter, which supports a fundamental mode at approximately 3.6 GHz and a higher-order mode at around 6.6 GHz, serving as channels for qubit reset and readout, respectively. In addition, an auxiliary mode is carefully embedded in our filter to provide intrinsic Purcell protec-

* These authors contributed equally to this work.

† kaixu@iphy.ac.cn

‡ zcxiang@iphy.ac.cn

§ hfan@iphy.ac.cn

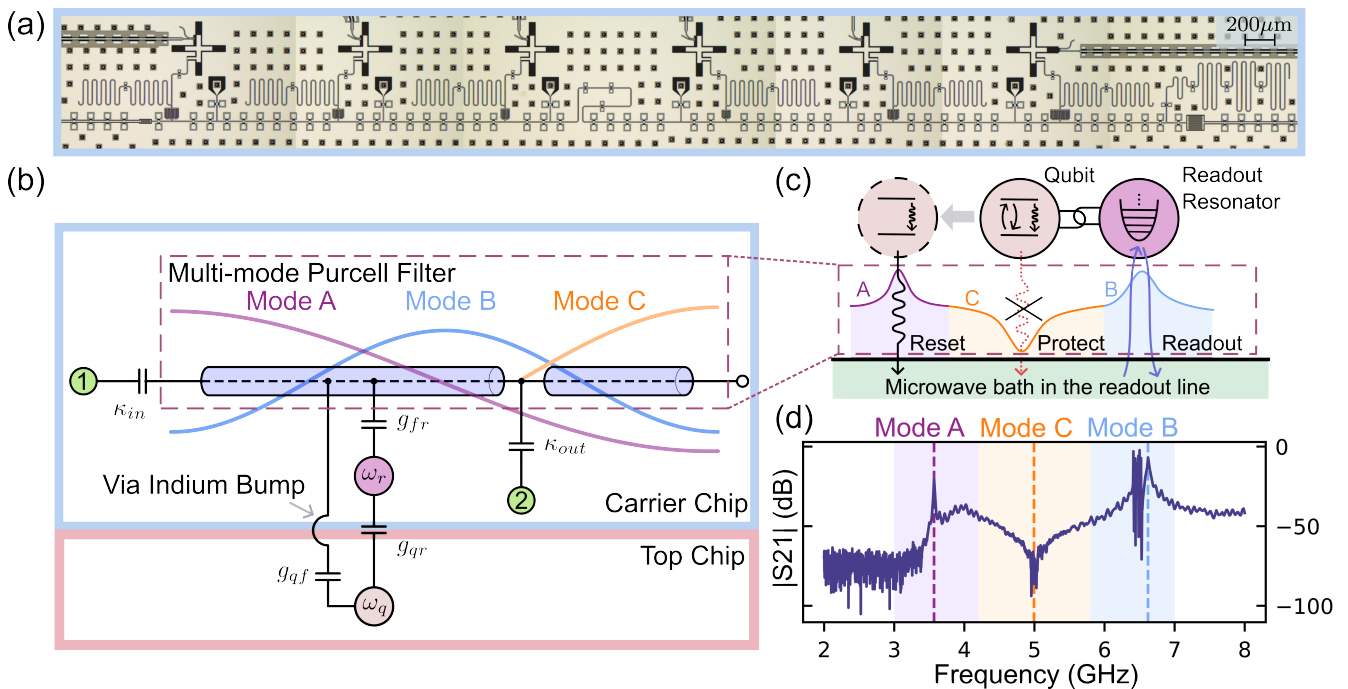


FIG. 1. (a) Photograph of the multi-mode Purcell filter shared by six readout resonators. The full device is a flip-chip superconducting quantum circuit consisting of a top qubit chip and a bottom carrier chip; the image shown here depicts the carrier chip. (b) Circuit model of the multi-mode filter. The filter is an open-circuited transmission-line resonator, where mode A is its fundamental mode and mode B is its second-order mode. Mode C is a $\lambda/4$ transmission-line stub that introduces a notch near 5 GHz. (c) Schematic illustration of the working principle of the multi-mode Purcell filter, which modifies the microwave bath seen by the qubit. Modes A and B serve as channels for qubit reset and readout, respectively, while mode C provides a notch filtering around qubit operation frequency, suppressing energy leakage. (d) Transmission spectrum S_{21} of the readout chain. The peak around 3.6 GHz corresponds to mode A, and the passband around 6.6 GHz corresponds to mode B. The dip around 5 GHz is the stopband produced by the quarter-wavelength stub (mode C). The readout resonators manifest themselves as dips within the passband constructed by mode B. The data are obtained using a vector network analyzer.

tion [29–31] for the qubit around its operation frequency. We experimentally demonstrate the performance of this multimode Purcell filter in a flip-chip superconducting circuit, in which we demonstrate a fast unconditional reset with residual excitation less than 1% within 220 ns, and a leakage reduction unit that selectively resets the transmon’s second excited state within 62 ns. The Purcell-limited relaxation time T_p of the qubit is also numerically simulated, predicting T_p exceeding 1 ms over a bandwidth of 800 MHz.

II. ENGINEERING A MULTIMODE PURCELL FILTER

Our protocol is based on a multi-mode filter with intrinsic Purcell protection, as shown in Fig. 1. Due to the multi-mode feature of the open-end transmission-line resonator, three carefully engineered modes are embedded in the filter. These modes, labeled as A, B, and C in Fig. 1, are responsible for the reset, readout, and additional Purcell protection, respectively. The fundamental mode of this open-end transmission-line resonator is mode A, whose resonant frequency $\omega_A/2\pi = 3.6$ GHz is

lower than the maximum frequency of the qubit. As a result, we can reset the qubit by tuning down its frequency to that of mode A, by which the qubit energy is first transferred to mode A and then rapidly dissipates due to the large leakage rate of the filter. Mode B is the second-order mode of the filter, which has a resonant frequency $\omega_B/2\pi = 6.6$ GHz, corresponding to the readout frequency. Through this mode, readout pulse injected from the input feedline can interact with the readout resonator and gain information about the qubit state. Finally, by moving the output capacitor to the position $\lambda_q/4$ away from the open end of the filter, a quarter-wavelength stub (mode C) is constructed, which performs as a stopband (see Fig. 1(d)) at qubit frequency and thus suppresses the Purcell decay through the filter. In other words, mode C in this distributed filter resonator corresponds to the electromagnetic mode that shows a voltage node at the position of the output capacitor. In this way, mode C can be decoupled from the microwave bath in the readout line. If the frequency of mode C is designed to be around that of the qubit, qubit energy leakage through the output capacitor can be suppressed, and the Purcell-limited relaxation time of the qubit can be greatly enhanced.

In summary, modes A, B, and C together construct a specific environment that can be used for qubit readout, reset, and providing additional Purcell protection, as can be seen from the transmission spectrum shown in Fig. 1(d) and the calculated Purcell-limited relaxation time shown in Fig. 4.

The experimental realization of the aforementioned multimode Purcell filter is carried out on a flip-chip superconducting circuit. As shown in Fig. 1(b), the qubits are fabricated on the top chip, while the readout resonators and the multimode Purcell filter are fabricated on the carrier chip. To characterize the performance of the multimode Purcell filter, the transmission spectrum S_{21} between the input and output ports of the readout chain is measured using a vector network analyzer, and the result is plotted in Fig. 1(d). The peak around 3.6 GHz is the first-order mode (i.e., mode A) of this open-end transmission-line resonator filter, and another peak around 6.6 GHz corresponds to the second-order mode (i.e., mode B) of the filter. The dips located around the peak of mode B are manifestations of the readout resonators whose frequencies are placed within the passband of the filter. While modes A and B perform themselves as peaks in the transmission spectrum, mode C contributes to a stopband around 5 GHz in the transmission spectrum, which prevents energy around this frequency from radiating to the readout line. In this way, additional Purcell protection can be added to the qubit that is tuned into the stopband built by mode C. By fitting the S21 data with the equation derived from input-output theory, the parameters of these modes can be extracted, and the results are listed in Table I (see Appendix B for details).

III. UNCONDITIONAL RESET USING THE FUNDAMENTAL MODE OF THE FILTER

An important property of our multimode Purcell filter is that its fundamental mode (mode A) at 3.6 GHz can be exploited to reset the qubit unconditionally. As shown in Fig. 1(b), the qubit in our architecture is coupled to the filter mode through direct capacitive coupling and indirect coupling mediated by the readout resonator. Note that the indirect coupling is quite weak, since mode A is detuned from the readout resonator by approximately 3 GHz. As a result, the direct coupling is necessary for implementing qubit reset via mode A. Since the frequency of mode A is lower than the transition frequency $\omega_{eg}/2\pi$

TABLE I. The frequency and linewidth of modes A, B obtained from the fit to the transmission spectrum shown in Fig. 1(d). Mode A and mode B are fitted individually, and the fit function is calculated using input-output formalism. See Appendix B for more details.

$\omega_A/2\pi$ (GHz)	$\kappa_A/2\pi$ (MHz)	$\omega_B/2\pi$ (GHz)	$\kappa_B/2\pi$ (MHz)
3.567	5.4	6.583	20.2

of the qubit, the qubit can be tuned to be resonant with mode A by direct flux tuning. In this way, the energy of the qubit can be swapped to the filter mode, and then rapidly dissipates due to the relatively large linewidth of the filter. In addition to resetting the first excited state $|e\rangle$ into the ground state $|g\rangle$, this method can be extended to reset both the $|e\rangle$ and the $|f\rangle$ of the qubit by cascading the f-e and e-g reset pulse, which bring the f-e transition and the e-g transition into resonance with mode A successively.

We use the pulse sequence shown in Fig. 2(a) to characterize the reset protocol described above. The qubit is optionally excited to $|e\rangle$ immediately before applying the reset pulse, and during the reset pulse the qubit is rapidly tuned to the reset frequency $\omega_{rst,e}$ for the duration of $t_{rst,e}$ and then tuned back. After that, the final state of the qubit is extracted by dispersive measurement. We scan the reset frequency $\omega_{rst,e}$ and the reset time $t_{rst,e}$, and measure the resulting qubit state. The result is plotted in Fig. 2(b). We can see that the optimal reset frequency is around 3.585 GHz (dark dashed line in Fig. 2(b)), which coincides with the first transmission peak of the S21 spectrum shown in Fig. 1(d) and Table I.

We adopt the reset frequency $\omega_{rst,e}/2\pi = 3.585$ GHz obtained in Fig. 2(b), calibrate the reset pulse shape, and then characterize the final state population $P_{g(e),e}$ ($P_{i,j}$ is defined as the $|i\rangle$ population of the transmon initialized in $|j\rangle$) as a function of the reset time $t_{rst,e}$ (see Fig. 2(c)). The residual excitation $1 - P_{g,e}$ is also computed and shown in Fig. 2(d). The result shows that the residual excitation can be reduced to less than 1% within 220ns. Here, the $1 - P_{g,e}$ versus time can be described by [16]

$$p_e = \begin{cases} \text{if } |g_{qf}| < \kappa_f/4 : \\ e^{-\kappa_f t/2} \left[\cosh(M_1 t) + \frac{\kappa_f}{4M_1} \sinh(M_1 t) \right]^2 ; \\ \text{if } |g_{qf}| = \kappa_f/4 : \\ e^{-\kappa_f t/2} (\kappa_f t/4 + 1)^2 ; \\ \text{if } |g_{qf}| > \kappa_f/4 : \\ e^{-\kappa_f t/2} \left[\cos(M_2 t) + \frac{\kappa_f}{4M_2} \sin(M_2 t) \right]^2 , \end{cases} \quad (1)$$

where $\kappa_f/2\pi$ is the linewidth of the filter mode, $g_{qf}/2\pi$ is the coupling strength between the qubit and the filter, $M_1 = \sqrt{\kappa_f^2 - 16|g_{qf}|^2}/4$ and $M_2 = \sqrt{16|g_{qf}|^2 - \kappa_f^2}/4$. Depending on the filter linewidth $\kappa_f/2\pi$ and the coupling strength $g_{qf}/2\pi$, three different regimes are possible, corresponding to overdamped, critically damped, and underdamped oscillations. The result shown in Fig. 2(d) corresponds to the underdamped regime where $g_{qf} > \kappa_f/4$. From the fit of the data using Eq. (1), we get the filter (mode A) linewidth $\kappa_f/2\pi = 8.5$ MHz and the coupling strength $g_{qf}/2\pi = 3.9$ MHz. From the fit, we also extract the steady-state residual excitation $P_{exc}^{s.s} = 0.8\%$, which is mainly caused by the readout error.

Next, we demonstrate that the above reset scheme can be extended to reset both the $|e\rangle$ and the $|f\rangle$ of the qubit by cascading the f-e and e-g reset pulses. To ex-

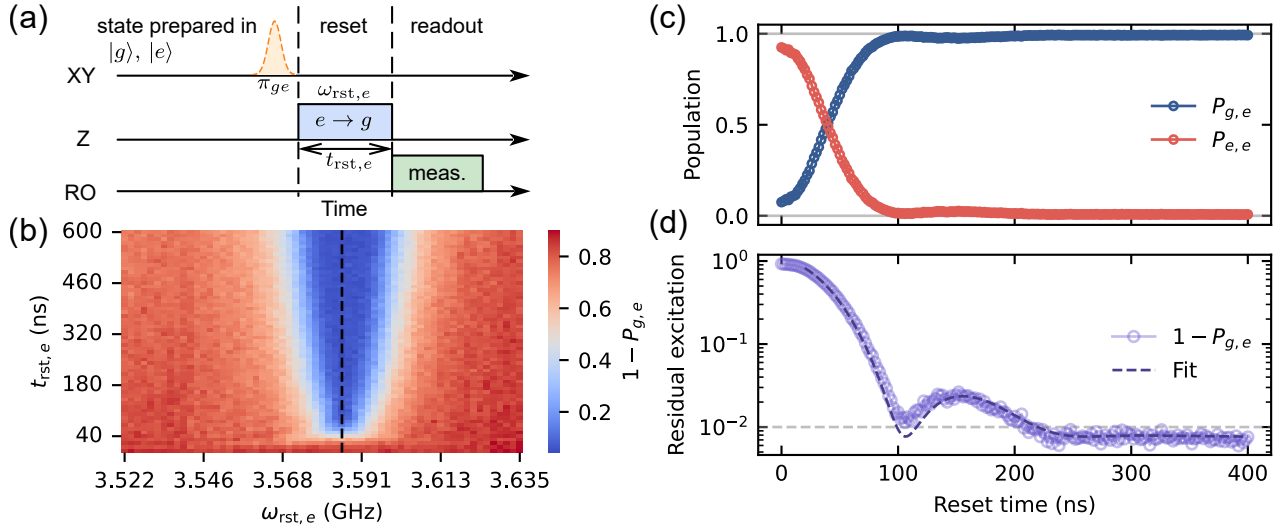


FIG. 2. Fast unconditional reset via the fundamental mode of the filter. (a) Schematic of the pulse sequence used to characterize the reset protocol. (b) Reset error $1 - P_{g,e}$ versus the reset frequency $\omega_{rst,e}/2\pi$ and the reset time $t_{rst,e}$. The optimal reset frequency $\omega_{rst,e}/2\pi$ is found to be 3.585 GHz (dark dashed line). (c)(d) The qubit population $P_{g(e)}$ and the residual excitation $1 - P_{g,e}$ versus the reset time $t_{rst,e}$. The qubit is first prepared in $|e\rangle$, and the reset frequency $\omega_{rst,e}/2\pi$ is chosen to be 3.585 GHz (dark dashed line in Fig. 2(b)). 15000 shots were taken per point. The purple dashed line is the fit using Eq. (1). The horizontal dashed line corresponds to $1 - P_{g,e} = 1\%$, and the residual excitation $1 - P_{g,e}$ is all below 1% for reset time $t_{rst,e} > 220$ ns.

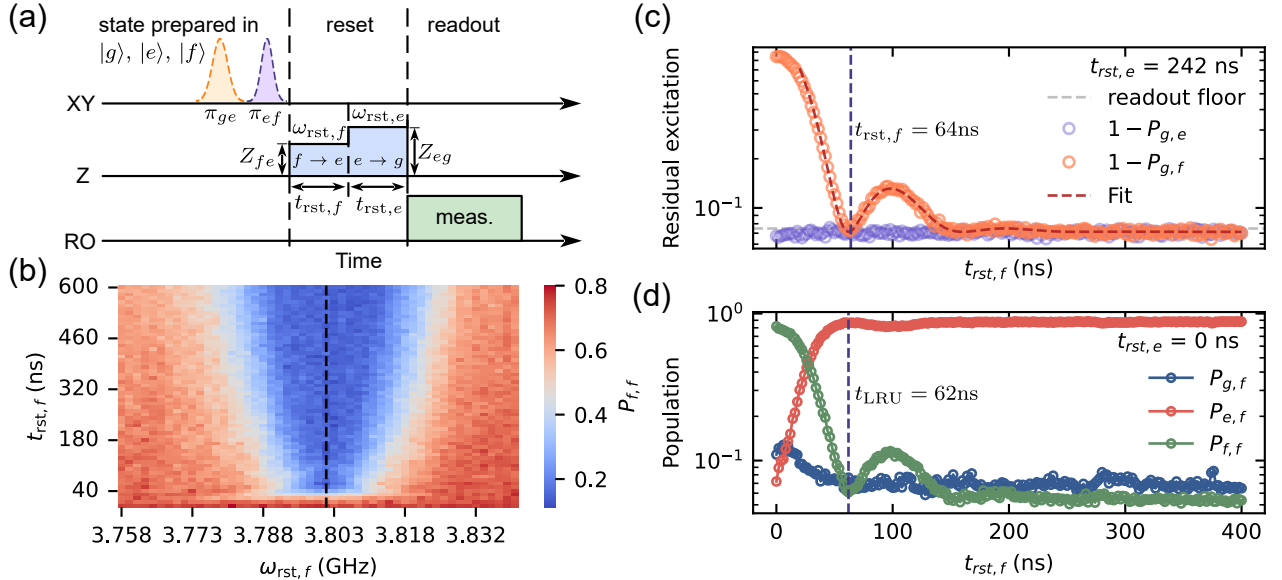


FIG. 3. Demonstration of the f-e cascaded reset scheme. (a) Pulse sequence used to reset both the first and second excited states of a transmon qubit. (b) The landscape of $P_{f,f}$ versus the f-e reset time $t_{rst,f}$ and the flux amplitude Z_{fe} . The optimal $\omega_{rst,f}/2\pi$ used to reset the $|f\rangle$ is found to be 3.801 GHz (dark dashed line). (c) The residual excitation $1 - P_{g,f(e)}$ versus the reset time $t_{rst,f}$, with $\omega_{rst,f}/2\pi = 3.801$ GHz, $\omega_{rst,e}/2\pi = 3.585$ GHz, and $t_{rst,e} = 242$ ns. $1 - P_{g,f}$ reaches its first minimum at $t_{rst,f} = 64$ ns (the vertical purple dashed line). The red dashed line is the fit to Eq. (1). The readout floor $1 - F_0$ is indicated by the horizontal dashed line. (d) The resulting population of a transmon initialized in $|f\rangle$ after an LRU operation, where $t_{rst,e} = 0$, $\omega_{rst,f}/2\pi = 3.801$ GHz, and $t_{rst,f}$ is swept. The $P_{f,f}$ reaches its first minimum at $t_{rst,f} = 62$ ns (the vertical purple dashed line).

tend the scheme to reset the second-excited state $|f\rangle$, we first apply a Z pulse with amplitude Z_{fe} (the corresponding e-g transition frequency of the transmon is labelled as $\omega_{rst,f}/2\pi$) to bring $\omega_{fe}/2\pi$ into resonance with mode

A for a duration of $t_{rst,f}$, and then apply a second Z pulse with amplitude Z_{eg} (the corresponding e-g transition frequency is labelled as $\omega_{rst,e}/2\pi$) to bring $\omega_{eg}/2\pi$ into resonance with mode A for a duration of $t_{rst,e}$. We

benchmark the efficiency of this cascaded reset pulse using the procedure shown in Fig. 3(a). To find a suitable $\omega_{\text{rst},f}/2\pi$ to reset the $|f\rangle$, we vary $\omega_{\text{rst},f}/2\pi$ while keeping $\omega_{\text{rst},e}/2\pi = 3.585$ GHz (which is the optimal e-g reset frequency found in Fig. 2(b)). The landscape of $P_{f,f}$ versus $t_{\text{rst},f}$ and $\omega_{\text{rst},f}/2\pi$ is shown in Fig. 3(b), indicating the optimal $\omega_{\text{rst},f}/2\pi$ to reset the $|f\rangle$ is around 3.801 GHz (dark dashed line in Fig. 3(b)). This $\omega_{\text{rst},f}/2\pi$ corresponds to $\omega_{fe}/2\pi \approx \omega_{\text{rst},f}/2\pi - E_C/h = 3.590$ GHz, which coincides with the resonance frequency of mode A.

With the optimal f-e and e-g reset frequencies obtained in Fig. 3(b) and Fig. 2(b), we then measure the dependence of reset error on $t_{\text{rst},f}$ for the cases when the qubit is initialized to $|e\rangle$ or $|f\rangle$. The result is presented in Fig. 3(c). We set $t_{\text{rst},e} = 242$ ns, which is enough to reset $|e\rangle$. As a result, the $|e\rangle$ reset error $1 - P_{g,e}$ shown in Fig. 3(c) already reaches its steady value around the readout floor and shows negligible dependence on the f-e reset time $t_{\text{rst},f}$. Next, we focus on the $|f\rangle$ reset error $1 - P_{g,f}$. Similar to the e-g reset process shown in Fig. 2, the $1 - P_{g,f}$ manifests oscillating decay over $t_{\text{rst},f}$, meaning the f-e reset process is also in the underdamped regime. Here, $1 - P_{g,f}$ reaches its first minimal (7.3%) at $t_{\text{rst},f} = 64$ ns (the vertical dash line in Fig. 3(c)). This means a f-e-g cascaded reset gate unconditionally resetting both $|e\rangle$ and $|f\rangle$ can be achieved in $(64+242)$ ns = 306 ns. The $1 - P_{g,f}$ data are fitted using Eq. (1) (the fit curve is depicted as the red dashed line in Fig. 3(c)), yielding $\kappa'_f/2\pi = 9.1$ MHz, $g'_{qf}/2\pi = 5.6$ MHz, and the steady-state residual excitation $P_{\text{exc},f}^{\text{s.s}} = 7.1\%$. $P_{\text{exc},f}^{\text{s.s}}$ is mainly limited by the qutrit readout error. Compared to the fitting result, $\kappa_f/2\pi$ and $g_{qf}/2\pi$, obtained in the e-g reset (see Fig. 2), here we have $\kappa'_f/\kappa_f \approx 1$ and $g'_{qf}/g_{qf} \approx \sqrt{2}$, which agrees with the theoretical prediction [32]. The consistency between these two fitting results demonstrates the reliability of our experimental results. Note that the filter linewidth $\kappa_f(\kappa'_f)$ obtained from fitting the reset curve shows a slight discrepancy compared to that derived from the S21 curve fitting (see the κ_A in Table I). The results obtained from the S21 curve fitting may exhibit certain distortions since it is difficult to consider the effects of all the components in the readout chain.

In addition to the f-e-g cascaded reset scheme described above, the relatively small (compared to the transmon anharmonicity) linewidth of mode A allows us to reset the $|f\rangle$ without damping the $|e\rangle$, which provides a means for implementing the LRU operation that selectively resets the second excited state. Here, the LRU operation can be derived from the f-e-g cascaded reset pulses shown in Fig. 3(a), by setting $t_{\text{rst},e} = 0$ ns and only keeping the f-e reset pulse. We sweep the $t_{\text{rst},f}$ and measure the transmon state population after the LRU operation. As shown in Fig. 3(d), the LRU operation can be completed in 62 ns with a residual $|f\rangle$ population of 6.1%. This relatively large residual population is mainly due to the qutrit readout error.

Compared to other reset schemes that rely on complex

pulse sequences and require precise calibration, the above reset protocol shows advantages in simplicity and stability. The reset error remains within an acceptable range even when the Z pulse parameters slightly deviate from their optimal values. This robustness against noise and parameter drift makes it attractive for use in large-scale, multi-qubit processors with automotive control systems.

IV. INTRINSIC PURCELL PROTECTION

The qubit in our device has direct capacitive coupling with the filter and with its own readout resonator simultaneously. Although its idle frequency (4.5 GHz) is designed to be significantly detuned from both the filter modes and the resonator mode, the Purcell leakage induced by this multi-mode electromagnetic environment may still jeopardize the lifetime of the qubit [33]. To suppress this influence, an auxiliary mode (Mode C) is introduced to provide additional Purcell protection for the qubit, as described in Sec. II and illustrated in Fig. 1. The effect of this intrinsic Purcell protection will be discussed more quantitatively in this section.

We model the filter resonator using the distributed circuit shown in Fig. 4, where the filter resonator is separated into three sections with lengths l_{p1} , l_{p2} , and l_{p3} . Port 1 and port 2 represent the input and the output ports of the filter, respectively, while port 3 represents the qubit coupled to the filter. The intrinsic Purcell protection mentioned above can be understood as the blockade of signals transmitted between ports 2 and 3. To elucidate this point, we compute the transfer impedance $Z_{23}(\omega)$ between port 2 and port 3, and the solution is given by (see Appendix C for details)

$$Z_{23} = \frac{-jZ_0 \cos \beta l_{p1} \cos \beta l_{p3}}{\sin \beta l_{p3} \cos \beta l_{p1} - \cos [\beta (l_p - l_{p1})] \sin \beta l_{p1}}, \quad (2)$$

where $\beta = 2\pi/\lambda = \omega/v$ is the propagation constant, Z_0 is the characteristic impedance of the transmission line used as the filter resonator, and $l_p = l_{p1} + l_{p2} + l_{p3}$ is the total length of the filter resonator. This result shows that at frequency where $\cos \beta l_{p1} = 0$ or $\cos \beta l_{p3} = 0$, the transfer impedance between port 2 and port 3 is zero, which means the excitation of the qubit is decoupled with the output port of the filter. Here, l_{p3} is designed to be $\lambda_q/4$. As a result, the leakage channel between port 2 and port 3 is blocked at the qubit frequency, suppressing the Purcell decay of the qubit. If l_{p3} is set to 0, Eq. (2) degenerates back to the case where there is no intrinsic Purcell protection.

The T_1 bound limited by the Purcell effect can be calculated as [33, 34]

$$T_p = C_q / \text{Re}[Y(\omega_q)], \quad (3)$$

where C_q is the qubit capacitance, and $Y(\omega_q)$ is the admittance of the external electromagnetic environment as seen by the qubit. The role of the Purcell protection can

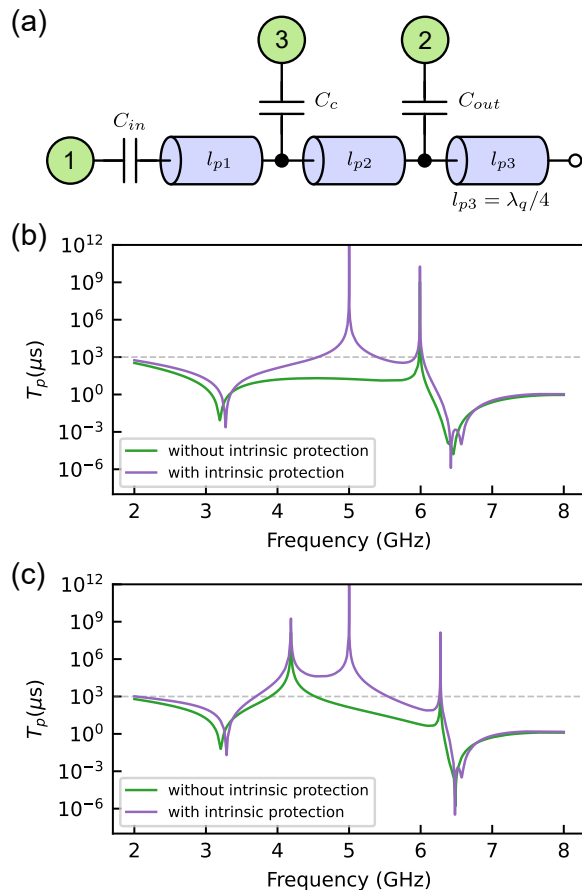


FIG. 4. Intrinsic Purcell protection of the filter. (a) Circuit model of the Purcell filter with additional notch filtering produced by the quarter-wavelength stub. Port 1 and Port 2 represent the input and output ports of the filter, respectively. Port 3 represents the qubit coupled to the filter. (b)(c) The Purcell-limited relaxation times T_p in the cases with and without the intrinsic Purcell filtering. (b) represents the case where $l_{p1}/(l_{p1} + l_{p2} + l_{p3}) \approx 0.01$, while (c) represents the case where $l_{p1}/(l_{p1} + l_{p2} + l_{p3}) \approx 0.39$. The data are obtained using numerical simulation of the circuit in LTspice (see Appendix D for details).

be interpreted as a modification of the $Y(\omega_q)$. We calculate the Purcell-limited relaxation times T_p for the case with and without the intrinsic Purcell protection using Eq. (3) (see Appendix D for details), and the results are depicted in Fig. 4(b) and (c). We first focus on the result shown in Fig. 4(b), which shows that we achieve a Purcell-limited relaxation time T_p exceeding 1 ms over a bandwidth of 800 MHz (from 4.56 GHz to 5.39 GHz), and the T_p can be extended to over 1 s if the frequency of the protective notch coincides with the qubit transition frequency $\omega_{eg}/2\pi$. This is a great enhancement compared to the situation without intrinsic Purcell protection, where the T_p is all below $30 \mu s$ from 4.5 GHz to 5.5 GHz. Note that apart from the peak around 5 GHz generated by the $\lambda_q/4$ stub, T_p also exhibits an additional peak at approximately 6 GHz (see Fig. 4(b)). This T_p peak is formed by

the interference between the $C_{qr} - C_{fr}$ path and the C_{qf} path [35], which can also be used to construct additional Purcell protection.

Note that apart from the T_p peak at frequency where $\cos \beta l_{p3} = 0$, another T_p peak also exists at frequency where $\cos \beta l_{p1} = 0$, as shown in Eq. (3). In the simulation depicted in Fig. 4(b), we consider the case where $l_{p1}/(l_{p1} + l_{p2} + l_{p3}) \approx 0.01$, i.e., the coupling point is near the input port of the filter. Thus, the T_p peak corresponding to $\cos \beta l_{p1} = 0$ is located in a relatively high frequency range and cannot be seen in Fig. 4(b). To explore the T_p peak corresponding to $\cos \beta l_{p1} = 0$, we carry out another simulation where $l_{p1}/(l_{p1} + l_{p2} + l_{p3}) \approx 0.39$, and the results are depicted in Fig. 4(c). We can see that apart from the peaks that have been mentioned in Fig. 4(b), another T_p peak appears around 4.2 GHz, corresponding to the frequency where $\cos \beta l_{p1} = 0$. In this case, we achieve a Purcell-limited relaxation time T_p exceeding 1 ms over a bandwidth of about 2 GHz, by combining the intrinsic Purcell protection produced by both $\cos \beta l_{p1} = 0$ and $\cos \beta l_{p3} = 0$. But we need to keep in mind that the Purcell protection provided by $\cos \beta l_{p1} = 0$ depends on the position of the qubit-filter coupling point. As a result, a general protection provided by $\cos \beta l_{p3} = 0$ is still necessary for constructing a Purcell filter shared by multiple qubits.

In summary, the results above show that the Purcell protection provided by our multimode filter is sufficient for building qubits with T_1 above $100 \mu s$, and is compatible with the long-lived transmon qubits realized recently [36–40].

V. DISCUSSION

Our results demonstrate that distinct qubit operations—namely, fast unconditional reset and high-fidelity readout—can be realized using different-order modes of a single microwave resonator, thereby eliminating the need for additional on-chip components. This mode-efficient approach, implemented via a multi-mode Purcell filter, not only preserves qubit coherence through intrinsic Purcell protection, but also provides fast dissipative channels essential for active reset and leakage removal—key requirements for quantum error correction.

Using this multi-mode filter, we demonstrate rapid reset of the $|e\rangle$ and $|f\rangle$ states within 220 ns and 310 ns. In addition, an LRU operation that selectively resets the second excited state can be completed in 62 ns. Although we only demonstrate the reset protocol in which the qubit is simply tuned into resonance with the fundamental mode of the filter, other reset schemes using parametric modulations [16, 17] or adiabatic swap operations [15] are also feasible on our device. In the experiment described in Sec. III, the reset process is in the underdamped regime where $g_{qf} > \kappa_f/4$. To further improve the reset speed, the linewidth of the filter can be increased to reach the critically damped regime

$g_{qf} = \kappa_f/4$. The characterization of the reset error is mainly limited by the readout fidelity, which can be improved by optimizing the dispersive shift and the effective linewidth of the resonator to reach larger state separation [41, 42], introducing quantum-limited amplifiers [43–48], using a shelving scheme that exploits higher energy levels of the qubit [49–54], and implementing more sophisticated readout pulses [51, 55–57]. Further analysis of the readout performance is presented in Appendix E. Our multi-mode Purcell filter can be extended to a multi-stage configuration [58]. In this case, the filter can have a large passband for accommodating readout resonators, which is attractive for use in large-scale quantum processors.

Although higher-order modes in coplanar waveguide resonators are often considered parasitic and detrimental to coherence [33], our work shows that they can be systematically engineered into functional resources. By assigning separate roles to the fundamental and second-order modes of a single resonator, we demonstrate that multiple operations can be multiplexed onto a single component. This design principle—assigning distinct qubit functionalities to different-order modes of a single multi-mode resonator—opens a new direction for scaling up superconducting quantum processors, particularly in architectures constrained by wiring and footprint.

Note that the Purcell effect in the multi-mode environment should be carefully considered, and additional Purcell protection may be needed as in the case described in Sec. IV. On the other hand, the lossy fundamental mode of the filter on our device may also serve as a useful resource for research on dissipative systems [59].

ACKNOWLEDGEMENTS

This work was supported by the National Natural Science Foundation of China (Grants No. 92265207, No. T2121001, No. T2322030, No. 12122504, No. 12274142, No. 92365206, No. 12104055, No. 12475017), the Natural Science Foundation of Guangdong Province (Grant No. 2024A1515010398), the Innovation Program for Quantum Science and Technology (Grants No. 2021ZD0301800, No. 2021ZD0301802), the Beijing Nova Program (No. 20220484121). We thank the support from the Synergetic Extreme Condition User Facility (SECUF) in Huairou District, Beijing. Devices were made at the Nanofabrication Facilities at Institute of Physics, CAS in Beijing.

Appendix A: Device information and experimental setup

Our experiment is carried out on a flip-chip superconducting processor, consisting of lithographically patterned aluminum films on sapphire substrates. The transmon qubits are fabricated on the top chip, and the

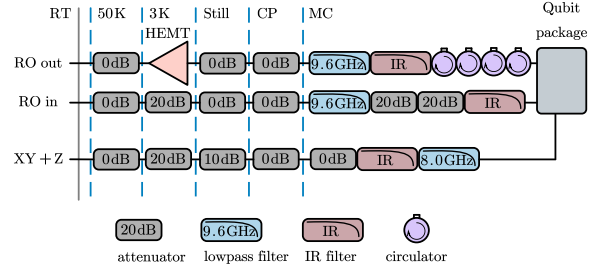


FIG. 5. Schematic of the wiring setup. The XY and Z control lines are integrated into one line. The readout pulse is sent in through the readout-input line (labelled as RO in), and the scattered signal containing state information leaves the chip through the readout-output line (labelled as RO out).

readout resonators, the multi-mode Purcell filter, and the control lines are integrated on the carrier chip. The details of device fabrication can be found in Ref. [60]. The qubit used in the experiment has a maximal e-g transition frequency $\omega_{eg}/2\pi = 4.621$ GHz and an anharmonicity $\alpha/2\pi = 211$ MHz. The qubit lifetime around the idle point is measured to be $T_1 = 58\mu\text{s}$. The readout resonator with frequency $\omega_r/2\pi = 6.486$ GHz is capacitively coupled to the qubit. The device is cooled down in a dilution refrigerator, and the wiring setup is shown in Fig. 5. Note that no quantum-limited amplifier is induced in the readout chain.

Appendix B: Extracting the parameters of the multimode filter

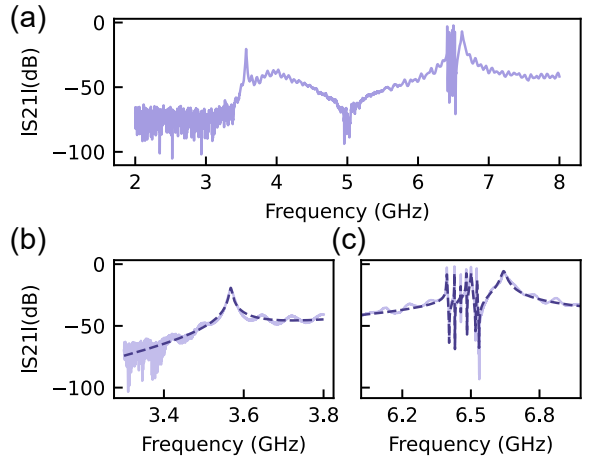


FIG. 6. (a) Transmission spectrum S_{21} of the readout chain collected by a vector network analyzer. (b) S_{21} of the frequency range covering the fundamental mode (Mode A) of the filter. (c) S_{21} of the frequency range covering the second-order mode (Mode B) of the filter. The dashed lines in (b) and (c) are the fits using Eq. (B1).

The transmission coefficient of a bandpass filter capacitively coupled to the readout line can be calculated following the input-output theory [61–63] and the results can be written as (here we assumed n readout resonators are coupled to the filter)

$$S_{21} = \frac{-j\kappa_f/2}{(j\Delta_{fd} + \kappa_f/2) + \sum_{i=1}^n |g_{fr,i}|^2 / (j\Delta_{r,i,d} + \gamma_{r,i}/2)}, \quad (\text{B1})$$

where $\kappa_f/2\pi$ is the linewidth of the filter, $\Delta_{fd} = \omega_f - \omega_d$ ($\Delta_{r,i,d} = \omega_{r,i} - \omega_d$) is the detuning between the filter (the readout resonators) and the probe tune, $g_{fr,i}$ is the coupling strength between the filter and the readout resonators, and $\gamma_{r,i}$ is induced to account for the intrinsic loss of the i th readout resonators. Although this formula just involves a single mode of the filter, it still well describes the transmission spectrum of our multimode filter, as long as the fundamental mode and the second-order mode of the filter are treated separately. To do that, the transmission data around the resonance frequency of the fundamental mode and the second-order mode are extracted and fitted to Eq. (B1) individually. To account for the influence of components like the amplifiers on the readout chain, a linear background is added to the fit function: $20 \log_{10} |S_{21}| + kf_d + b$. The fit curves are shown in Fig. 6(b) and (c), and the extracted parameters are listed in Table I.

Appendix C: The intrinsic notch filtering produced by the quarter-wavelength stub

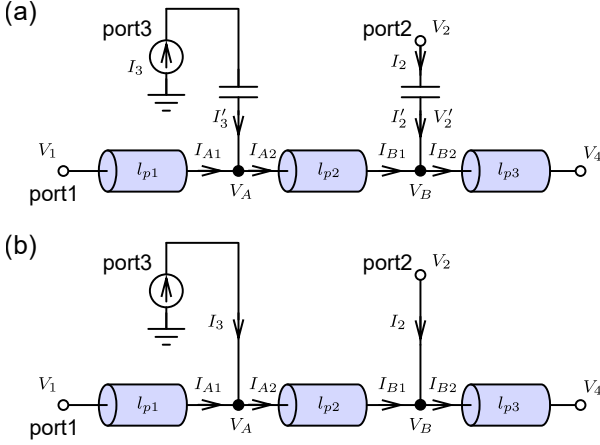


FIG. 7. (a) Distributed-circuit model of the filter with a quarter-wavelength stub. The Purcell filter is divided into three segments with lengths l_{p1} , l_{p2} and l_{p3} , respectively. The input and output ports of the filter are labeled as port 1 and port 2, respectively. Port 3 represents the qubit coupled to the filter. (a) can be simplified to (b) for the derivation of the intrinsic notch filtering described by Eq. (2).

As described in Sec. II and Sec. IV, by moving the output capacitor to the position $\lambda_q/4$ away from the

open end of the filter, a quarter-wavelength stub is constructed, which prevents the microwave signal whose frequency is around $\omega_q/2\pi$ dissipating into the readout line and provides the additional Purcell protection. This working principle can also be formulated by computing the transfer impedance $Z_{23} = \frac{V_2}{I_3} |_{I_k=0 \text{ for } k \neq 3}$ between the coupling point and the output port of the filter [30]. Here we will calculate the transfer impedance Z_{23} of the model in Fig. 7(a) following the theory in [64].

Since the transmission(ABCD) matrix of a series capacitance C is

$$T = \begin{pmatrix} 1 & Z \\ 0 & 1 \end{pmatrix} = \begin{pmatrix} 1 & \frac{1}{j\omega C} \\ 0 & 1 \end{pmatrix}, \quad (\text{C1})$$

the voltages and currents at point A and B in Fig. 7(a) are given by

$$I'_3 = I_3, \quad (\text{C2})$$

$$V'_2 = V_2 + I_2 / (j\omega C_{out}) = V_2. \quad (\text{C3})$$

As a result, the model in Fig. 7(a) can be simplified to Fig. 7(b) when formulating the transfer impedance Z_{23} . The input impedance of a lossless transmission line terminated in an open-circuited end can be written as

$$\begin{aligned} Z_{in}(z) &= \frac{V(z)}{I(z)} = Z_0 \frac{Z_L + jZ_0 \tan \beta z}{Z_0 + jZ_L \tan \beta z} \Big|_{Z_L=+\infty} \\ &= Z_0 \frac{1}{j \tan \beta z} \end{aligned} \quad (\text{C4})$$

by which we get the input impedance of point A(B) looking towards the open-circuited end 1(4) in Fig. 7(b):

$$\frac{V_A}{I_{A1}} = Z_0 \frac{1}{j \tan \beta l_{p1}}, \quad (\text{C5})$$

$$\frac{V_B}{I_{B2}} = Z_0 \frac{1}{j \tan \beta l_{p3}}. \quad (\text{C6})$$

And Kirchhoff's Current Law gives

$$I_{B2} = I_{A1} + I_3 + I_2 = I_{A1} + I_3. \quad (\text{C7})$$

Then, combining the above relations, the transfer impedance Z_{23} can be written as

$$\begin{aligned} Z_{23} &= \frac{V_2}{I_3} = \frac{V_B}{I_3} = \frac{V_B}{I_{B2} - I_{A1}} = \frac{V_B/I_{B2}}{1 - I_{A1}/I_{B2}} \\ &= \frac{Z_0 \frac{1}{j \tan \beta l_{p3}}}{1 - I_{A1}/I_{B2}} = \frac{Z_0 \frac{1}{j \tan \beta l_{p3}}}{1 - \frac{V_A \tan \beta l_{p1}}{V_B \tan \beta l_{p3}}}. \end{aligned} \quad (\text{C8})$$

The voltage distribution on a lossless transmission line terminated in an open circuit is

$$\begin{aligned} V(z) &= V_L^+ (e^{j\beta z} + \Gamma_L e^{-j\beta z}) = V_L^+ (e^{j\beta z} + e^{-j\beta z}) \\ &= 2V_L^+ \cos \beta z, \end{aligned} \quad (\text{C9})$$

where z is the distance from the open end. Following this equation, we get

$$\frac{V_A}{V_B} = \frac{\cos[\beta(l_{p2} + l_{p3})]}{\cos\beta l_{p3}}. \quad (\text{C10})$$

By substituting Eq. (C10) into the Z_{23} described in Eq. (C8), we finally obtain

$$\begin{aligned} Z_{23} &= \frac{Z_0 \frac{1}{j \tan \beta l_{p3}}}{1 - \frac{V_A}{V_B} \frac{\tan \beta l_{p1}}{\tan \beta l_{p3}}} = \frac{Z_0 \frac{1}{j \tan \beta l_{p3}}}{1 - \frac{\cos[\beta(l_{p2} + l_{p3})]}{\cos \beta l_{p3}} \frac{\tan \beta l_{p1}}{\tan \beta l_{p3}}} \\ &= \frac{-j Z_0 \cos \beta l_{p1} \cos \beta l_{p3}}{\sin \beta l_{p3} \cos \beta l_{p1} - \cos[\beta(l_p - l_{p1})] \sin \beta l_{p1}} \end{aligned} \quad (\text{C11})$$

which is the Eq. (2) in the main text.

Appendix D: Simulation of the Purcell-limited relaxation times

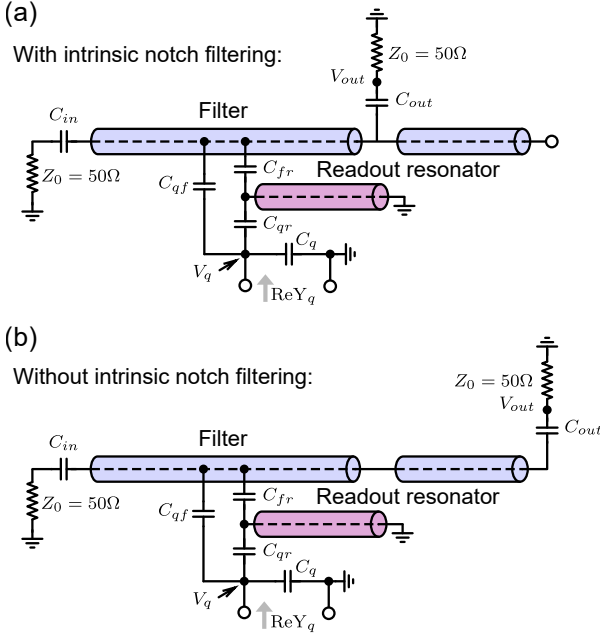


FIG. 8. Circuit models used for numerical simulation. (a) and (b) are the situations with and without the intrinsic notch filtering produced by the quarter-wavelength stub, respectively.

The Purcell decay rate of a transmon qubit coupled to a lossy linear mode off-resonantly is given by $\Gamma = \kappa(g/\Delta)^2$ [32], where g is the coupling strength between the qubit and the linear mode, κ is the effective linewidth of the mode, and Δ is the detuning. However, this formula only considers a single EM mode and fails to describe the Purcell decay rate of the qubit here, which is damped in a multi-mode environment provided by our multi-mode filter. To estimate the Purcell decay rate of the qubit in our device, we follow an alternative method

in which the classical admittance Y_q of the external circuit seen by the qubit is calculated and thus the Purcell-limited relaxation time T_p is given by Eq. (3) in the main text. Here, $Y(\omega_q)$ is calculated using numerical simulation of the circuit in LTspice. The circuit models are shown in Fig. 8(a) and Fig. 8(b), which correspond to the situations with and without the intrinsic Purcell protection, respectively. In the simulation, the qubit is replaced by a voltage source V_q . By measuring the corresponding source current I_q , the real part of the admittance is simply given by $\text{Re}Y_q = \text{Re}(I_q/V_q)$. However, this method does not work well around the frequency range where $\text{Re}Y_q$ is relatively small. In this case, the alternative method is to measure the voltage across the output port V_{out} , and the $\text{Re}Y_q$ is calculated by [29]

$$\text{Re}[Y_q(\omega)] = \frac{1}{Z_0} \left| \frac{V_{out}(\omega)}{V_q(\omega)} \right|^2, \quad (\text{D1})$$

where Z_0 is the characteristic impedance of the output line. This formula lies in the fact that the power supplied by the current source is nearly equal to the power transmitted to the output port. Some of the power is transmitted to the input port here, but this part of the energy is quite small compared to that transmitted to the output port due to the asymmetric design of the capacitors ($C_{out} \gg C_{in}$). Following this way, we calculate the T_p of the qubit with and without the intrinsic Purcell protection, and obtain the results shown in Fig. 4 in the main text.

Appendix E: Readout characterization and error analysis

The readout assignment probability matrices of the qubit used in the reset experiment are presented in Fig. 9. The $|g\rangle$ and $|e\rangle$ assignment errors in the case of two-level state discrimination are $\varepsilon_0 = 1.08\%$ and $\varepsilon_1 = 8.86\%$, respectively. To analyze the source of the readout errors, we further divide the errors into two categories: the separation error and the state error [65]. The separation error reflects the intrinsic signal-to-noise ratio of the dispersed photons and can be captured by the overlap area of the Gaussian fits to the signal clusters in the IQ plane. Here, the separation errors of the two-level state discrimination are found to be $\varepsilon_{s,0} = 0.38\%$ and $\varepsilon_{s,1} = 0.08\%$. The remaining part $\varepsilon_{t,0(1)} = \varepsilon_{0(1)} - \varepsilon_{s,0(1)}$ is the state error caused by state-transition events before or during the readout process. The finite T_1 of the qubit is a common source of the $|e\rangle$ state error $\varepsilon_{t,1}$. For a qubit with $T_1 = 50 \mu\text{s}$ and a readout integration time $\tau_m = 2 \mu\text{s}$, the bound of ε_1 can be estimated as

$$\begin{aligned} \varepsilon_{T_1} &= 1 - \exp(-\tau_m/T_1) \\ &\approx 1 - (1 - \tau_m/T_1) = \tau_m/T_1 = 4\%. \end{aligned} \quad (\text{E1})$$

The remaining part of the state error $\varepsilon_{t,1} - \varepsilon_{T_1}$ is mainly due to the measurement-induced state transition [28, 66].

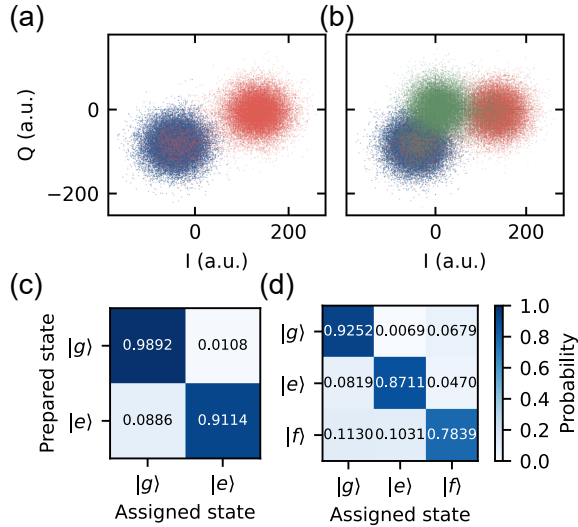


FIG. 9. Readout characterization. (a) and (b) are the IQ signals in the cases of the two-level state readout and the three-level state readout, respectively. The $|g\rangle$, $|e\rangle$, and $|f\rangle$ are represented by blue dots, red dots, and green dots, respectively. 30000 repetitions of the experiment are performed for each prepared state. The corresponding assignment probability matrices are presented in (c) and (d).

The $|g\rangle$ state error $\varepsilon_{t,0} = \varepsilon_0 - \varepsilon_{s,0} = 0.70\%$ may be caused by the thermal excitation. The thermal population and the corresponding effective temperature T_{eff} of the bath damping the qubit is given by the Maxwell-Boltzmann distribution [67]

$$p_e/p_g = \exp\left(-\frac{\hbar\omega_{eg}}{k_B T_{eff}}\right), \quad (E2)$$

where, $p_e(p_g)$ is the excited-state(ground-state) population of the qubit, $\omega_{eg}/2\pi$ is the e-g transition frequency of the qubit, \hbar is the reduced Planck constant and k_B is the Boltzmann constant. Here, p_e/p_g is 0.007/0.993 around 4.5 GHz, and the corresponding effective temperature T_{eff} is estimated to be 44 mK. Compared to the two-level state readout, the three-level state readout has relatively larger assignment errors, which is partly due to the relatively large overlap of these three clusters of states in the IQ plane, as shown in Fig. 9(b).

-
- [1] A. G. Fowler, M. Mariantoni, J. M. Martinis, and A. N. Cleland, Surface codes: Towards practical large-scale quantum computation, *Physical Review A* **86**, 032324 (2012).
- [2] C. J. Axline, L. D. Burkhardt, W. Pfaff, M. Zhang, K. Chou, P. Campagne-Ibarcq, P. Reinhold, L. Frunzio, S. M. Girvin, L. Jiang, M. H. Devoret, and R. J. Schoelkopf, On-demand quantum state transfer and entanglement between remote microwave cavity memories, *Nature Physics* **14**, 705 (2018).
- [3] P. Campagne-Ibarcq, E. Zalys-Geller, A. Narla, S. Shankar, P. Reinhold, L. Burkhardt, C. Axline, W. Pfaff, L. Frunzio, R. J. Schoelkopf, and M. H. Devoret, Deterministic Remote Entanglement of Superconducting Circuits through Microwave Two-Photon Transitions, *Physical Review Letters* **120**, 200501 (2018).
- [4] P. Kurpiers, P. Magnard, T. Walter, B. Royer, M. Pechal, J. Heinsoo, Y. Salathé, A. Akin, S. Storz, J.-C. Besse, S. Gasparinetti, A. Blais, and A. Wallraff, Deterministic quantum state transfer and remote entanglement using microwave photons, *Nature* **558**, 264 (2018).
- [5] N. Leung, Y. Lu, S. Chakram, R. K. Naik, N. Earnest, R. Ma, K. Jacobs, A. N. Cleland, and D. I. Schuster, Deterministic bidirectional communication and remote entanglement generation between superconducting qubits, *npj Quantum Information* **5**, 18 (2019).
- [6] P. Magnard, S. Storz, P. Kurpiers, J. Schär, F. Marxer, J. Lütolf, T. Walter, J.-C. Besse, M. Gabureac, K. Reuer, A. Akin, B. Royer, A. Blais, and A. Wallraff, Microwave Quantum Link between Superconducting Circuits Housed in Spatially Separated Cryogenic Systems, *Physical Review Letters* **125**, 260502 (2020).
- [7] L. D. Burkhardt, J. D. Teoh, Y. Zhang, C. J. Axline, L. Frunzio, M. Devoret, L. Jiang, S. Girvin, and R. Schoelkopf, Error-Detected State Transfer and Entanglement in a Superconducting Quantum Network, *PRX Quantum* **2**, 030321 (2021).
- [8] Y. Zhong, H.-S. Chang, A. Bienfait, É. Dumur, M.-H. Chou, C. R. Conner, J. Grebel, R. G. Povey, H. Yan, D. I. Schuster, and A. N. Cleland, Deterministic multi-qubit entanglement in a quantum network, *Nature* **590**, 571 (2021).
- [9] J. Niu, L. Zhang, Y. Liu, J. Qiu, W. Huang, J. Huang, H. Jia, J. Liu, Z. Tao, W. Wei, Y. Zhou, W. Zou, Y. Chen, X. Deng, X. Deng, C. Hu, L. Hu, J. Li, D. Tan, Y. Xu, F. Yan, T. Yan, S. Liu, Y. Zhong, A. N. Cleland, and D. Yu, Low-loss interconnects for modular superconducting quantum processors, *Nature Electronics* **6**, 235 (2023).
- [10] S. Storz, J. Schär, A. Kulikov, P. Magnard, P. Kurpiers, J. Lütolf, T. Walter, A. Copetudo, K. Reuer, A. Akin, J.-C. Besse, M. Gabureac, G. J. Norris, A. Rosario, F. Martin, J. Martinez, W. Amaya, M. W. Mitchell, C. Abellan, J.-D. Bancal, N. Sangouard, B. Royer, A. Blais, and A. Wallraff, Loophole-free Bell inequality violation with superconducting circuits, *Nature* **617**, 265 (2023).
- [11] J. Qiu, Y. Liu, L. Hu, Y. Wu, J. Niu, L. Zhang, W. Huang, Y. Chen, J. Li, S. Liu, Y. Zhong, L. Duan, and D. Yu, Deterministic quantum state and gate teleportation between distant superconducting chips, *Science Bulletin* **70**, 351 (2025).
- [12] J. Qiu, Z. Zhang, Z. Wang, L. Zhang, Y. Zhou, X. Sun, J. Zhang, X. Linpeng, S. Liu, J. Niu, Y. Zhong, and D. Yu, A thermal-noise-resilient microwave quantum net-

- work traversing 4 K (2025), [arXiv:2503.01133 \[quant-ph\]](https://arxiv.org/abs/2503.01133).
- [13] M. D. Reed, B. R. Johnson, A. A. Houck, L. DiCarlo, J. M. Chow, D. I. Schuster, L. Frunzio, and R. J. Schoelkopf, Fast reset and suppressing spontaneous emission of a superconducting qubit, *Applied Physics Letters* **96**, 203110 (2010).
- [14] P. Magnard, P. Kurpiers, B. Royer, T. Walter, J.-C. Besse, S. Gasparinetti, M. Pechal, J. Heinsoo, S. Storz, A. Blais, and A. Wallraff, Fast and Unconditional All-Microwave Reset of a Superconducting Qubit, *Physical Review Letters* **121**, 060502 (2018).
- [15] M. McEwen, D. Kafri, Z. Chen, J. Atalaya, K. J. Satzinger, C. Quintana, P. V. Klimov, D. Sank, C. Gidney, A. G. Fowler, F. Arute, K. Arya, B. Buckley, B. Burkett, N. Bushnell, B. Chiaro, R. Collins, S. Demura, A. Dunsworth, C. Erickson, B. Foxen, M. Giustina, T. Huang, S. Hong, E. Jeffrey, S. Kim, K. Kechedzhi, F. Kostritsa, P. Laptev, A. Megrant, X. Mi, J. Mutus, O. Naaman, M. Neeley, C. Neill, M. Niu, A. Paler, N. Redd, P. Roushan, T. C. White, J. Yao, P. Yeh, A. Zalcman, Y. Chen, V. N. Smelyanskiy, J. M. Martinis, H. Neven, J. Kelly, A. N. Korotkov, A. G. Petukhov, and R. Barends, Removing leakage-induced correlated errors in superconducting quantum error correction, *Nature Communications* **12**, 1761 (2021).
- [16] Y. Zhou, Z. Zhang, Z. Yin, S. Huai, X. Gu, X. Xu, J. Allcock, F. Liu, G. Xi, Q. Yu, H. Zhang, M. Zhang, H. Li, X. Song, Z. Wang, D. Zheng, S. An, Y. Zheng, and S. Zhang, Rapid and unconditional parametric reset protocol for tunable superconducting qubits, *Nature Communications* **12**, 5924 (2021).
- [17] G. Kim, A. Butler, V. S. Ferreira, X. Zhang, A. Hadley, E. Kim, and O. Painter, Fast Unconditional Reset and Leakage Reduction of a Tunable Superconducting Qubit via an Engineered Dissipative Bath (2024), [arXiv:2411.02950](https://arxiv.org/abs/2411.02950).
- [18] J. Ding, Y. Li, H. Wang, G. Xue, T. Su, C. Wang, W. Sun, F. Li, Y. Zhang, Y. Gao, J. Peng, Z. H. Jiang, Y. Yu, H. Yu, and F. Yan, Multipurpose architecture for fast reset and protective readout of superconducting qubits, *Physical Review Applied* **23**, 014012 (2025).
- [19] P. Aliferis and B. M. Terhal, Fault-Tolerant Quantum Computation for Local Leakage Faults (2006), [arXiv:quant-ph/0511065](https://arxiv.org/abs/quant-ph/0511065).
- [20] F. Battistel, B. Varbanov, and B. Terhal, Hardware-Efficient Leakage-Reduction Scheme for Quantum Error Correction with Superconducting Transmon Qubits, *PRX Quantum* **2**, 030314 (2021).
- [21] X. Yang, J. Chu, Z. Guo, W. Huang, Y. Liang, J. Liu, J. Qiu, X. Sun, Z. Tao, J. Zhang, J. Zhang, L. Zhang, Y. Zhou, W. Guo, L. Hu, J. Jiang, Y. Liu, X. Linpeng, T. Chen, Y. Chen, J. Niu, S. Liu, Y. Zhong, and D. Yu, Coupler-Assisted Leakage Reduction for Scalable Quantum Error Correction with Superconducting Qubits, *Physical Review Letters* **133**, 170601 (2024).
- [22] T. Thorbeck, A. McDonald, O. Lanes, J. Blair, G. Keefe, A. A. Stabile, B. Royer, L. C. G. Govia, and A. Blais, High-fidelity gates in a transmon using bath engineering for passive leakage reset (2024), [arXiv:2411.04101](https://arxiv.org/abs/2411.04101).
- [23] M. D. Reed, L. DiCarlo, S. E. Nigg, L. Sun, L. Frunzio, S. M. Girvin, and R. J. Schoelkopf, Realization of three-qubit quantum error correction with superconducting circuits, *Nature* **482**, 382 (2012).
- [24] Google Quantum AI, Z. Chen, K. J. Satzinger, J. Atalaya, A. N. Korotkov, A. Dunsworth, D. Sank, C. Quintana, M. McEwen, R. Barends, P. V. Klimov, S. Hong, C. Jones, A. Petukhov, D. Kafri, S. Demura, B. Burkett, C. Gidney, A. G. Fowler, A. Paler, H. Putterman, I. Aleiner, F. Arute, K. Arya, R. Babbush, J. C. Bardin, A. Bengtsson, A. Bourassa, M. Broughton, B. B. Buckley, D. A. Buell, N. Bushnell, B. Chiaro, R. Collins, W. Courtney, A. R. Derk, D. Eppens, C. Erickson, E. Farhi, B. Foxen, M. Giustina, A. Greene, J. A. Gross, M. P. Harrigan, S. D. Harrington, J. Hilton, A. Ho, T. Huang, W. J. Huggins, L. B. Ioffe, S. V. Isakov, E. Jeffrey, Z. Jiang, K. Kechedzhi, S. Kim, A. Kitaev, F. Kostritsa, D. Landhuis, P. Laptev, E. Lucero, O. Martin, J. R. McClean, T. McCourt, X. Mi, K. C. Miao, M. Mohseni, S. Montazeri, W. Mruczkiewicz, J. Mutus, O. Naaman, M. Neeley, C. Neill, M. Newman, M. Y. Niu, T. E. O'Brien, A. Opremcak, E. Ostby, B. Pató, N. Redd, P. Roushan, N. C. Rubin, V. Shvarts, D. Strain, M. Szalay, M. D. Trevithick, B. Villalonga, T. White, Z. J. Yao, P. Yeh, J. Yoo, A. Zalcman, H. Neven, S. Boixo, V. Smelyanskiy, Y. Chen, A. Megrant, and J. Kelly, Exponential suppression of bit or phase errors with cyclic error correction, *Nature* **595**, 383 (2021).
- [25] S. Krinner, N. Lacroix, A. Remm, A. Di Paolo, E. Genois, C. Leroux, C. Hellings, S. Lazar, F. Swiadek, J. Herrmann, G. J. Norris, C. K. Andersen, M. Müller, A. Blais, C. Eichler, and A. Wallraff, Realizing repeated quantum error correction in a distance-three surface code, *Nature* **605**, 669 (2022).
- [26] Google Quantum AI, R. Acharya, I. Aleiner, R. Allen, T. I. Andersen, M. Ansmann, F. Arute, K. Arya, A. Asfaw, J. Atalaya, R. Babbush, D. Bacon, J. C. Bardin, J. Basso, A. Bengtsson, S. Boixo, G. Bortoli, A. Bourassa, J. Bovaird, L. Brill, M. Broughton, B. B. Buckley, D. A. Buell, T. Burger, B. Burkett, N. Bushnell, Y. Chen, Z. Chen, B. Chiaro, J. Cogan, R. Collins, P. Conner, W. Courtney, A. L. Crook, B. Curtin, D. M. Debroy, A. Del Toro Barba, S. Demura, A. Dunsworth, D. Eppens, C. Erickson, L. Faoro, E. Farhi, R. Fatemi, L. Flores Burgos, E. Forati, A. G. Fowler, B. Foxen, W. Giang, C. Gidney, D. Gilboa, M. Giustina, A. Grajales Dau, J. A. Gross, S. Habegger, M. C. Hamilton, M. P. Harrigan, S. D. Harrington, O. Higgott, J. Hilton, M. Hoffmann, S. Hong, T. Huang, A. Huff, W. J. Huggins, L. B. Ioffe, S. V. Isakov, J. Iveland, E. Jeffrey, Z. Jiang, C. Jones, P. Juhas, D. Kafri, K. Kechedzhi, J. Kelly, T. Khattar, M. Khezri, M. Kieferová, S. Kim, A. Kitaev, P. V. Klimov, A. R. Klots, A. N. Korotkov, F. Kostritsa, J. M. Kreikebaum, D. Landhuis, P. Laptev, K.-M. Lau, L. Laws, J. Lee, K. Lee, B. J. Lester, A. Lill, W. Liu, A. Locharla, E. Lucero, F. D. Malone, J. Marshall, O. Martin, J. R. McClean, T. McCourt, M. McEwen, A. Megrant, B. Meurer Costa, X. Mi, K. C. Miao, M. Mohseni, S. Montazeri, A. Morvan, E. Mount, W. Mruczkiewicz, O. Naaman, M. Neeley, C. Neill, A. Nersisyan, H. Neven, M. Newman, J. H. Ng, A. Nguyen, M. Nguyen, M. Y. Niu, T. E. O'Brien, A. Opremcak, J. Platt, A. Petukhov, R. Potter, L. P. Pryadko, C. Quintana, P. Roushan, N. C. Rubin, N. Saei, D. Sank, K. Sankaragomathi, K. J. Satzinger, H. F. Schurkus, C. Schuster, M. J. Shearn, A. Shorter, V. Shvarts, J. Skrzynny, V. Smelyanskiy, W. C. Smith, G. Sterling, D. Strain, M. Szalay, A. Torres, G. Vi-

- dal, B. Villalonga, C. Vollgraf Heidweiller, T. White, C. Xing, Z. J. Yao, P. Yeh, J. Yoo, G. Young, A. Zalcman, Y. Zhang, and N. Zhu, Suppressing quantum errors by scaling a surface code logical qubit, *Nature* **614**, 676 (2023).
- [27] Google Quantum AI and Collaborators, R. Acharya, D. A. Abanin, L. Aghababaie-Beni, I. Aleiner, T. I. Andersen, M. Ansmann, F. Arute, K. Arya, A. Asfaw, N. Astrakhantsev, J. Atalaya, R. Babbush, D. Bacon, B. Ballard, J. C. Bardin, J. Bausch, A. Bengtsson, A. Bilmes, S. Blackwell, S. Boixo, G. Bortoli, A. Bourassa, J. Bovaird, L. Brill, M. Broughton, D. A. Browne, B. Buchea, B. B. Buckley, D. A. Buell, T. Burger, B. Burkett, N. Bushnell, A. Cabrera, J. Campero, H.-S. Chang, Y. Chen, Z. Chen, B. Chiaro, D. Chik, C. Chou, J. Claes, A. Y. Cleland, J. Cogan, R. Collins, P. Conner, W. Courtney, A. L. Crook, B. Curtin, S. Das, A. Davies, L. De Lorenzo, D. M. Debroy, S. Demura, M. Devoret, A. Di Paolo, P. Donohoe, I. Drozdov, A. Dunsworth, C. Earle, T. Edlich, A. Eickbusch, A. M. Elbag, M. Elzouka, C. Erickson, L. Faoro, E. Farhi, V. S. Ferreira, L. F. Burgos, E. Forati, A. G. Fowler, B. Foxen, S. Ganjam, G. Garcia, R. Gasca, É. Genois, W. Giang, C. Gidney, D. Gilboa, R. Gosula, A. G. Dau, D. Graumann, A. Greene, J. A. Gross, S. Habegger, J. Hall, M. C. Hamilton, M. Hansen, M. P. Harrigan, S. D. Harrington, F. J. H. Heras, S. Heslin, P. Heu, O. Higgott, G. Hill, J. Hilton, G. Holland, S. Hong, H.-Y. Huang, A. Huff, W. J. Huggins, L. B. Ioffe, S. V. Isakov, J. Iveland, E. Jeffrey, Z. Jiang, C. Jones, S. Jordan, C. Joshi, P. Juhas, D. Kafri, H. Kang, A. H. Karamlou, K. Kechedzhi, J. Kelly, T. Khairé, T. Khattar, M. Khezri, S. Kim, P. V. Klimov, A. R. Klots, B. Kobrin, P. Kohli, A. N. Korotkov, F. Kostritsa, R. Kothari, B. Kozlovskii, J. M. Kreikebaum, V. D. Kurilovich, N. Lacroix, D. Landhuis, T. Lange-Dei, B. W. Langley, P. Laptev, K.-M. Lau, L. Le Guevel, J. Ledford, J. Lee, K. Lee, Y. D. Lensky, S. Leon, B. J. Lester, W. Y. Li, Y. Li, A. T. Lill, W. Liu, W. P. Livingston, A. Locharla, E. Lucero, D. Lundahl, A. Lunt, S. Madhuk, F. D. Malone, A. Maloney, S. Mandrà, J. Manyika, L. S. Martin, O. Martin, S. Martin, C. Maxfield, J. R. McClean, M. McEwen, S. Meeks, A. Megrant, X. Mi, K. C. Miao, A. Mieszala, R. Molavi, S. Molina, S. Montazeri, A. Morvan, R. Movassagh, W. Mruczkiewicz, O. Naaman, M. Neeley, C. Neill, A. Nersisyan, H. Neven, M. Newman, J. H. Ng, A. Nguyen, M. Nguyen, C.-H. Ni, M. Y. Niu, T. E. O'Brien, W. D. Oliver, A. Opremcak, K. Ottosson, A. Petukhov, A. Pizzuto, J. Platt, R. Potter, O. Pritchard, L. P. Pryadko, C. Quintana, G. Ramachandran, M. J. Reagor, J. Redding, D. M. Rhodes, G. Roberts, E. Rosenberg, E. Rosenfeld, P. Roushan, N. C. Rubin, N. Saei, D. Sank, K. Sankaragomathi, K. J. Satzinger, H. F. Schurkus, C. Schuster, A. W. Senior, M. J. Shearn, A. Shorter, N. Shutty, V. Shvarts, S. Singh, V. Sivak, J. Skrzynny, S. Small, V. Smelyanskiy, W. C. Smith, R. D. Somma, S. Springer, G. Sterling, D. Strain, J. Suchard, A. Szasz, A. Szein, D. Thor, A. Torres, M. M. Torunbalci, A. Vaishnav, J. Vargas, S. Vdovichev, G. Vidal, B. Villalonga, C. V. Heidweiller, S. Waltman, S. X. Wang, B. Ware, K. Weber, T. Weidel, T. White, K. Wong, B. W. K. Woo, C. Xing, Z. J. Yao, P. Yeh, B. Ying, J. Yoo, N. Yosri, G. Young, A. Zalcman, Y. Zhang, N. Zhu, and N. Zobrist, Quantum error correction below the surface code threshold, *Nature* **638**, 920 (2025).
- [28] M. F. Dumas, B. Groleau-Paré, A. McDonald, M. H. Muñoz-Arias, C. Lledó, B. D'Anjou, and A. Blais, Measurement-Induced Transmon Ionization, *Physical Review X* **14**, 041023 (2024).
- [29] Y. Sunada, S. Kono, J. Ilves, S. Tamate, T. Sugiyama, Y. Tabuchi, and Y. Nakamura, Fast readout and reset of a superconducting qubit coupled to a resonator with an intrinsic purcell filter, *Physical Review Applied* **17**, 044016 (2022).
- [30] P. A. Spring, L. Milanovic, Y. Sunada, S. Wang, A. F. Van Loo, S. Tamate, and Y. Nakamura, Fast Multiplexed Superconducting-Qubit Readout with Intrinsic Purcell Filtering Using a Multiconductor Transmission Line, *PRX Quantum* **6**, 020345 (2025).
- [31] A. Yen, Y. Ye, K. Peng, J. Wang, G. Cunningham, M. Gingras, B. M. Niedzielski, H. Stickler, K. Serniak, M. E. Schwartz, and K. P. O'Brien, Interferometric Purcell suppression of spontaneous emission in a superconducting qubit, *Physical Review Applied* **23**, 024068 (2025).
- [32] J. Koch, T. M. Yu, J. Gambetta, A. A. Houck, D. I. Schuster, J. Majer, A. Blais, M. H. Devoret, S. M. Girvin, and R. J. Schoelkopf, Charge-insensitive qubit design derived from the Cooper pair box, *Physical Review A* **76**, 042319 (2007).
- [33] A. A. Houck, J. A. Schreier, B. R. Johnson, J. M. Chow, J. Koch, J. M. Gambetta, D. I. Schuster, L. Frunzio, M. H. Devoret, S. M. Girvin, and R. J. Schoelkopf, Controlling the Spontaneous Emission of a Superconducting Transmon Qubit, *Physical Review Letters* **101**, 080502 (2008).
- [34] D. Esteve, M. H. Devoret, and J. M. Martinis, Effect of an arbitrary dissipative circuit on the quantum energy levels and tunneling of a Josephson junction, *Physical Review B* **34**, 158 (1986).
- [35] N. T. Bronn, E. Magesan, N. A. Masluk, J. M. Chow, J. M. Gambetta, and M. Steffen, Reducing spontaneous emission in circuit quantum electrodynamics by a combined readout/filter technique, *IEEE Transactions on Applied Superconductivity* **25**, 1 (2015).
- [36] A. P. M. Place, L. V. H. Rodgers, P. Mundada, B. M. Smitham, M. Fitzpatrick, Z. Leng, A. Premkumar, J. Bryon, A. Vrajitoarea, S. Sussman, G. Cheng, T. Madhavan, H. K. Babla, X. H. Le, Y. Gang, B. Jäck, A. Geynis, N. Yao, R. J. Cava, N. P. de Leon, and A. A. Houck, New material platform for superconducting transmon qubits with coherence times exceeding 0.3 milliseconds, *Nature Communications* **12**, 1779 (2021).
- [37] C. Wang, X. Li, H. Xu, Z. Li, J. Wang, Z. Yang, Z. Mi, X. Liang, T. Su, C. Yang, G. Wang, W. Wang, Y. Li, M. Chen, C. Li, K. Linghu, J. Han, Y. Zhang, Y. Feng, Y. Song, T. Ma, J. Zhang, R. Wang, P. Zhao, W. Liu, G. Xue, Y. Jin, and H. Yu, Towards practical quantum computers: Transmon qubit with a lifetime approaching 0.5 milliseconds, *npj Quantum Information* **8**, 3 (2022).
- [38] M. Tuokkola, Y. Sunada, H. Kivijärvi, L. Grönberg, J.-P. Kaikkonen, V. Vesterinen, J. Govenius, and M. Möttönen, Methods to achieve near-millisecond energy relaxation and dephasing times for a superconducting transmon qubit (2024), [arXiv:2407.18778](https://arxiv.org/abs/2407.18778) [quant-ph].

- [39] M. Bal, A. A. Murthy, S. Zhu, F. Crisa, X. You, Z. Huang, T. Roy, J. Lee, D. V. Zanten, R. Pilipenko, I. Nekrashevich, A. Lunin, D. Bafia, Y. Krasnikova, C. J. Kopas, E. O. Lachman, D. Miller, J. Y. Mutus, M. J. Reagor, H. Cansizoglu, J. Marshall, D. P. Pappas, K. Vu, K. Yadavalli, J.-S. Oh, L. Zhou, M. J. Kramer, F. Lecocq, D. P. Goronzy, C. G. Torres-Castanedo, P. G. Pritchard, V. P. Dravid, J. M. Rondinelli, M. J. Bedzyk, M. C. Hersam, J. Zasadzinski, J. Koch, J. A. Sauls, A. Romanenko, and A. Grassellino, Systematic improvements in transmon qubit coherence enabled by niobium surface encapsulation, *npj Quantum Information* **10**, 43 (2024).
- [40] M. P. Bland, F. Bahrami, J. G. C. Martinez, P. H. Prestegard, B. M. Smitham, A. Joshi, E. Hedrick, A. Pakpour-Tabrizi, S. Kumar, A. Jindal, R. D. Chang, A. Yang, G. Cheng, N. Yao, R. J. Cava, N. P. de Leon, and A. A. Houck, 2D transmons with lifetimes and coherence times exceeding 1 millisecond (2025), [arXiv:2503.14798](https://arxiv.org/abs/2503.14798) [quant-ph].
- [41] T. Walter, P. Kurpiers, S. Gasparinetti, P. Magnard, A. Potočnik, Y. Salathé, M. Pechal, M. Mondal, M. Oppliger, C. Eichler, and A. Wallraff, Rapid High-Fidelity Single-Shot Dispersive Readout of Superconducting Qubits, *Physical Review Applied* **7**, 054020 (2017).
- [42] A. Blais, A. L. Grimsmo, S. M. Girvin, and A. Wallraff, Circuit quantum electrodynamics, *Reviews of Modern Physics* **93**, 025005 (2021).
- [43] C. M. Caves, Quantum limits on noise in linear amplifiers, *Physical Review D* **26**, 1817 (1982).
- [44] M. A. Castellanos-Beltran, K. D. Irwin, G. C. Hilton, L. R. Vale, and K. W. Lehnert, Amplification and squeezing of quantum noise with a tunable Josephson metamaterial, *Nature Physics* **4**, 929 (2008).
- [45] C. Eichler, Y. Salathe, J. Mlynek, S. Schmidt, and A. Wallraff, Quantum-Limited Amplification and Entanglement in Coupled Nonlinear Resonators, *Physical Review Letters* **113**, 110502 (2014).
- [46] J. Y. Mutus, T. C. White, R. Barends, Y. Chen, Z. Chen, B. Chiaro, A. Dunsworth, E. Jeffrey, J. Kelly, A. Megrant, C. Neill, P. J. J. O'Malley, P. Roushan, D. Sank, A. Vainsencher, J. Wenner, K. M. Sundqvist, A. N. Cleland, and J. M. Martinis, Strong environmental coupling in a Josephson parametric amplifier, *Applied Physics Letters* **104**, 263513 (2014).
- [47] C. Macklin, K. O'Brien, D. Hover, M. E. Schwartz, V. Bolkhovskiy, X. Zhang, W. D. Oliver, and I. Siddiqi, A near-quantum-limited Josephson traveling-wave parametric amplifier, *Science* **350**, 307 (2015).
- [48] R. Kaufman, T. White, M. I. Dykman, A. Iorio, G. Sterling, S. Hong, A. Opremcak, A. Bengtsson, L. Faoro, J. C. Bardin, T. Burger, R. Gasca, and O. Naaman, Josephson parametric amplifier with Chebyshev gain profile and high saturation, *Physical Review Applied* **20**, 054058 (2023).
- [49] S. S. Elder, C. S. Wang, P. Reinhold, C. T. Hann, K. S. Chou, B. J. Lester, S. Rosenblum, L. Frunzio, L. Jiang, and R. J. Schoelkopf, High-Fidelity Measurement of Qubits Encoded in Multilevel Superconducting Circuits, *Physical Review X* **10**, 011001 (2020).
- [50] F. Mallet, F. R. Ong, A. Palacios-Laloy, F. Nguyen, P. Bertet, D. Vion, and D. Esteve, Single-shot qubit readout in circuit quantum electrodynamics, *Nature Physics* **5**, 791 (2009).
- [51] L. Chen, H.-X. Li, Y. Lu, C. W. Warren, C. J. Križan, S. Kosen, M. Rommel, S. Ahmed, A. Osman, J. Biznárová, A. Fadavi Roudsari, B. Lienhard, M. Caputo, K. Grigoras, L. Grönberg, J. Govenius, A. F. Kockum, P. Delsing, J. Bylander, and G. Tancredi, Transmon qubit readout fidelity at the threshold for quantum error correction without a quantum-limited amplifier, *npj Quantum Information* **9**, 26 (2023).
- [52] C. Wang, F.-M. Liu, H. Chen, Y.-F. Du, C. Ying, J.-W. Wang, Y.-H. Huo, C.-Z. Peng, X. Zhu, M.-C. Chen, C.-Y. Lu, and J.-W. Pan, 99.9%-fidelity in measuring a superconducting qubit (2024), [arXiv:2412.13849](https://arxiv.org/abs/2412.13849) [quant-ph].
- [53] T. Jiang, J. Cai, J. Huang, N. Zhou, Y. Zhang, J. Bei, G. Cai, S. Cao, F. Chen, J. Chen, K. Chen, X. Chen, X. Chen, Z. Chen, Z. Chen, Z. Chen, W. Chu, H. Deng, Z. Deng, P. Ding, X. Ding, Z. Ding, S. Dong, B. Fan, D. Fan, Y. Fu, D. Gao, L. Ge, J. Gui, C. Guo, S. Guo, X. Guo, L. Han, T. He, L. Hong, Y. Hu, H.-L. Huang, Y.-H. Huo, Z. Jiang, H. Jin, Y. Leng, D. Li, D. Li, F. Li, J. Li, J. Li, J. Li, J. Li, N. Li, S. Li, W. Li, Y. Li, Y. Li, F. Liang, X. Liang, N. Liao, J. Lin, W. Lin, D. Liu, H. Liu, M. Liu, X. Liu, X. Liu, Y. Liu, H. Lou, Y. Ma, L. Meng, H. Mou, K. Nan, B. Nie, M. Nie, J. Ning, L. Niu, W. Peng, H. Qian, H. Rong, T. Rong, H. Shen, Q. Shen, H. Su, F. Su, C. Sun, L. Sun, T. Sun, Y. Sun, Y. Tan, J. Tan, L. Tang, W. Tu, J. Wang, B. Wang, C. Wang, C. Wang, C. Wang, J. Wang, L. Wang, R. Wang, S. Wang, X. Wang, X. Wang, X. Wang, Y. Wang, Z. Wei, J. Wei, D. Wu, G. Wu, J. Wu, Y. Wu, S. Xie, L. Xin, Y. Xu, C. Xue, K. Yan, W. Yang, X. Yang, Y. Yang, Y. Ye, Z. Ye, C. Ying, J. Yu, Q. Yu, W. Yu, X. Zeng, C. Zha, S. Zhan, F. Zhang, H. Zhang, K. Zhang, W. Zhang, Y. Zhang, Y. Zhang, L. Zhang, G. Zhao, P. Zhao, X. Zhao, Y. Zhao, Z. Zhao, L. Zheng, F. Zhou, L. Zhou, N. Zhou, S. Zhou, S. Zhou, Z. Zhou, C. Zhu, Q. Zhu, G. Zou, H. Zou, Q. Zhang, C.-Y. Lu, C.-Z. Peng, X. Yuan, M. Gong, X. Zhu, and J.-W. Pan, Generation of 95-qubit genuine entanglement and verification of symmetry-protected topological phases (2025), [arXiv:2505.01978](https://arxiv.org/abs/2505.01978) [quant-ph].
- [54] A. Zhang, H. Xie, Y. Gao, J.-N. Yang, Z. Bao, Z. Zhu, J. Chen, N. Wang, C. Zhang, J. Zhong, S. Xu, K. Wang, Y. Wu, F. Jin, X. Zhu, Y. Zou, Z. Tan, Z. Cui, F. Shen, T. Li, Y. Han, Y. He, G. Liu, J. Shen, H. Wang, Y. Wang, H. Dong, J. Deng, H. Li, Z. Wang, C. Song, Q. Guo, P. Zhang, Y. Li, and H. Wang, Demonstrating quantum error mitigation on logical qubits (2025), [arXiv:2501.09079](https://arxiv.org/abs/2501.09079) [quant-ph].
- [55] D. T. McClure, H. Paik, L. S. Bishop, M. Steffen, J. M. Chow, and J. M. Gambetta, Rapid Driven Reset of a Qubit Readout Resonator, *Physical Review Applied* **5**, 011001 (2016).
- [56] M. Jerger, F. Motzoi, Y. Gao, C. Dickel, L. Buchmann, A. Bengtsson, G. Tancredi, C. W. Warren, J. Bylander, D. DiVincenzo, R. Barends, and P. A. Bushev, Dispersive Qubit Readout with Intrinsic Resonator Reset (2024), [arXiv:2406.04891](https://arxiv.org/abs/2406.04891) [quant-ph].
- [57] F. Swiadek, R. Shillito, P. Magnard, A. Remm, C. Hellings, N. Lacroix, Q. Ficheux, D. C. Zanuz, G. J. Norris, A. Blais, S. Krinner, and A. Wallraff, Enhancing Dispersive Readout of Superconducting Qubits through Dynamic Control of the Dispersive Shift: Experiment and Theory, *PRX Quantum* **5**, 040326 (2024).

- [58] H. Yan, X. Wu, A. Lingenfelter, Y. J. Joshi, G. Andersson, C. R. Conner, M.-H. Chou, J. Grebel, J. M. Miller, R. G. Povey, H. Qiao, A. A. Clerk, and A. N. Cleland, Broadband bandpass Purcell filter for circuit quantum electrodynamics, *Applied Physics Letters* **123**, 134001 (2023).
- [59] P.-R. Han, F. Wu, X.-J. Huang, H.-Z. Wu, C.-L. Zou, W. Yi, M. Zhang, H. Li, K. Xu, D. Zheng, H. Fan, J. Wen, Z.-B. Yang, and S.-B. Zheng, Exceptional Entanglement Phenomena: Non-Hermiticity Meeting Non-classicality, *Physical Review Letters* **131**, 260201 (2023).
- [60] Z.-H. Liu, Y. Liu, G.-H. Liang, C.-L. Deng, K. Chen, Y.-H. Shi, T.-M. Li, L. Zhang, B.-J. Chen, C.-P. Fang, D. Feng, X.-Y. Gu, Y. He, K. Huang, H. Li, H.-T. Liu, L. Li, Z.-Y. Mei, Z.-Y. Peng, J.-C. Song, M.-C. Wang, S.-L. Wang, Z. Wang, Y. Xiao, M. Xu, Y.-S. Xu, Y. Yan, Y.-H. Yu, W.-P. Yuan, J.-C. Zhang, J.-J. Zhao, K. Zhao, S.-Y. Zhou, Z.-A. Wang, X. Song, Y. Tian, F. Mintert, J. Knolle, R. Moessner, Y.-R. Zhang, P. Zhang, Z. Xiang, D. Zheng, K. Xu, H. Zhao, and H. Fan, Prethermalization by Random Multipolar Driving on a 78-Qubit Superconducting Processor (2025), [arXiv:2503.21553](https://arxiv.org/abs/2503.21553) [quant-ph].
- [61] O. Naaman and J. Aumentado, Synthesis of Parametrically Coupled Networks, *PRX Quantum* **3**, 020201 (2022).
- [62] E. A. Sete, J. M. Martinis, and A. N. Korotkov, Quantum theory of a bandpass Purcell filter for qubit readout, *Physical Review A* **92**, 012325 (2015).
- [63] J. Heinsoo, C. K. Andersen, A. Remm, S. Krinner, T. Walter, Y. Salathé, S. Gasparinetti, J.-C. Besse, A. Potočnik, A. Wallraff, and C. Eichler, Rapid High-fidelity Multiplexed Readout of Superconducting Qubits, *Physical Review Applied* **10**, 034040 (2018).
- [64] D. M. Pozar, *Microwave Engineering*, 4th ed.
- [65] D. Sank, *Fast, Accurate State Measurement in Superconducting Qubits*, Ph.D. thesis (2014).
- [66] M. Boissonneault, J. M. Gambetta, and A. Blais, Dispersive regime of circuit QED: Photon-dependent qubit dephasing and relaxation rates, *Physical Review A* **79**, 013819 (2009).
- [67] X. Y. Jin, A. Kamal, A. P. Sears, T. Gudmundsen, D. Hover, J. Miloshi, R. Slattery, F. Yan, J. Yoder, T. P. Orlando, S. Gustavsson, and W. D. Oliver, Thermal and Residual Excited-State Population in a 3D Transmon Qubit, *Physical Review Letters* **114**, 240501 (2015).